Symmetry-Driven Generation of Crystal Structures from Composition

Shi Yin[†,1,*] Jinming Mu,[2,*] Xudong Zhu,[1] and Linxin He[†2,1]

[1] *Institute of Artificial Intelligence, Hefei Comprehensive National Science Center, Hefei, Anhui, 230088, China*
[2] *Laboratory of Quantum Information, University of Science and Technology of China, Hefei, Anhui, 230026, China*

Crystal structure prediction (CSP), which aims to predict the three-dimensional atomic arrangement of a crystal from its composition, is central to materials discovery and mechanistic understanding. However, given the composition in a unit cell, existing methods struggle with the NP-hard combinatorial challenge of rigorous symmetry enforcement or rely on retrieving known templates, which inherently limits both physical fidelity and the ability to discover genuinely new materials. To solve this, we propose a symmetry-driven generative framework. Our approach leverages large language models to encode chemical semantics and directly generate fine-grained Wyckoff patterns from atomic stoichiometry, effectively circumventing the limitations inherent to database lookups. Crucially, to overcome the exponentially complex problem of combinatorial site assignments, we incorporate domain knowledge through an efficient, linear-complexity heuristic beam search algorithm that rigorously enforces algebraic consistency between site multiplicities and atomic stoichiometry. By integrating this symmetry-consistent template into a diffusion backbone, our approach constrains the stochastic generative trajectory to a physically valid geometric manifold. This framework achieves state-of-the-art performance across stability, uniqueness, and novelty (SUN) benchmarks, alongside superior matching performance, thereby establishing a new paradigm for the rigorous exploration of targeted crystallographic space which can be previously uncharted, with no reliance on a priori structural knowledge.

arXiv:2602.17176v3 [cond-mat.mtrl-sci] 7 Mar 2026

Crystalline materials are fundamental to modern technologies spanning energy, electronics, medicine, and aerospace, and advancing these sectors relies on identifying novel crystal structures with tailored properties [1–5]. The vastness of the compositional and structural parameter space presents a fundamental bottleneck for materials discovery. Conventional pipelines, guided by chemical intuition and constrained by costly computations and experiments [6, 7], are intrinsically inefficient at exploring this space at scale.

In recent years, artificial intelligence (AI), and deep learning-based generative models in particular, have emerged as a promising route to proposing candidate materials at scale, demonstrating superior generalization capabilities and significant advantages in computational efficiency [8–14]. Within this landscape, the crystal structure prediction (CSP) task [8, 10, 13], which seeks the three-dimensional arrangement of atoms in the unit cell from a given composition, plays a pivotal role in AI-driven materials design workflows [11]. Diffusion models have become the dominant architecture for 3D structure generation [15, 16], and, for the CSP task, diffusion-based approaches also deliver state-of-the-art performance [10, 14].

However, the CSP task is fundamentally governed by stringent crystallographic rules, imposing rigid constraints on the design methodology. Physically plausible crystal structures typically obey the symmetry constraints imposed by specific space groups, which strictly constrain the allowed Wyckoff positions, determining atomic multiplicities, site symmetries, and the relative arrangement of atoms within the unit cell. Only when the given chemical composition is mathematically consistent with the corresponding Wyckoff positions can physically reasonable crystal structures be obtained.

However, rigorously enforcing these physical constraints imposed by space groups remains a universal bottleneck across the entire CSP domain. Fundamentally, determining an exact combination of Wyckoff positions whose multiplicities perfectly align with the exact atom counts of a given composition in the unit cell constitutes an inherently NP-hard combinatorial optimization problem, characterized by an exponentially exploding search space. Current methods struggle to efficiently resolve this task, often resorting to partial compromises. For example, aiming at efficiently addressing site assignments, Xin *et al.* [17] introduces a search method for Wyckoff positions with a pruning strategy. However, the approach remains fundamentally a brute-force enumeration. As the number of atoms in the unit cell scales up, the possible integer partitions of these atoms into available Wyckoff orbits explode exponentially. Consequently, for large atomic systems containing dozens of atoms, this exhaustive search encounters a severe combinatorial explosion, rendering the enumeration computationally prohibitive. Furthermore, the approach lacks a likelihood-based ranking mechanism, making it practically impossible to identify the most physically plausible candidates from the massive, unguided pool of generated combinations.

Within the landscape of generative AI, existing methods also only partially circumvent this challenge. Early and generic 3D generative models, such as CDVAE [18] and DiffCSP [19], completely bypass this discrete combinatorial challenge. They operate directly on continuous coordinates and rely on neural networks to implicitly learn crystallographic symmetries, which leaves the generative trajectory unconstrained in an unimaginably vast search space. CrystaLLM [9] presents a text gen-

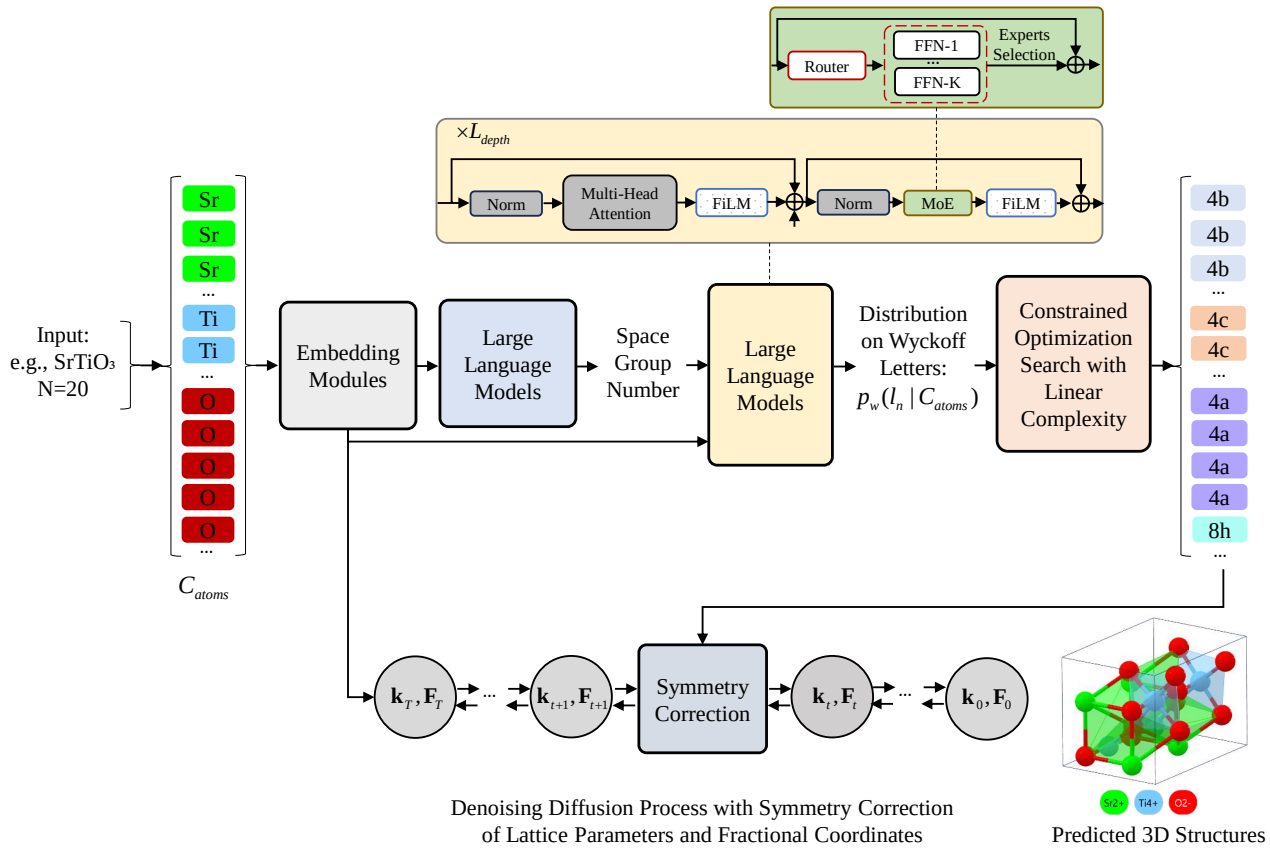

FIG. 1: Schematic of the proposed symmetry-driven generative framework.

eration framework autoregressively predicting Crystallographic Information File (CIF) formats; however, any generated symmetry or Wyckoff symbols are mere textual probabilistic outputs, entirely lacking algebraic or physical hard constraints. Some recent approaches condition the generator on a space group label [11, 14] but do not explicitly represent or enforce Wyckoff positions, so symmetry is only captured in a coarse global sense.

Moving beyond coarse global symmetry, several recent AI methods attempt to explicitly utilize and strictly enforce Wyckoff positions, yet they remain hindered by the intractable complexity of exact site assignments. While WyCryst [12] elegantly guides generation via Wyckoff-based latent representations, its soft-penalty sampling cannot guarantee strict stoichiometric alignment. Consequently, extracting 3D structures consistent with Wyckoff positions relies on post-hoc filtering, a process that can become computationally prohibitive given the NP-hard nature of combinatorial site assignments. CrystalFormer [20] presents a compelling framework representing crystals as Wyckoff sequences with logit masking for symmetry enforcement. While effective for generating structures within a given space group number, the final stoichiometry is an emergent outcome of the sampling process rather than a hard constraint. Since the model focuses on generative modeling, it does not employ an explicit constrained optimization mechanism to align site multiplicities with a given composition and atomic number in a cell. DiffCSP++ [10] goes further by enforcing strict space group symmetry defined by Wyckoff templates during the 3D material generation process. It employs two strategies for obtaining these templates: the first directly utilizes the ground-truth Wyckoff templates of the target material to guide structure generation. However, in practical CSP scenarios, these ground-truth templates are inherently unknown a priori. As an alternative, it relies on a retrieval-based approach, which assumes that a suitable space group and Wyckoff template are already known in the given lookup database. In practice, these templates are retrieved from existing structures via metric learning methods, such as CSPML [21]. However, restricting generation to retrieved templates confines the model to known symmetry patterns, thereby limiting its ability to discover genuinely new space-group and Wyckoff configurations for a given composition.

To address these fundamental limitations, we propose an efficient symmetry-driven generative framework, which enables the *ab initio* generation of fine-grained Wyckoff site assignments directly from composition and

atom counts, independent of any structural priors, as depicted in Fig. 1. Building upon the probabilistic distributions inferred by large language models (LLMs), we explicitly overcome the intractable exponential complexity of combinatorial site assignments discussed above by designing an efficient heuristic constrained-optimization search. This algorithm drastically compresses the time complexity from an exponential scale down to a linear scale, rendering the search computationally tractable while rigorously enforcing algebraic consistency between site multiplicities and atomic stoichiometry without relying on computationally prohibitive brute-force enumeration. Crucially, the predicted symmetries are then imposed as hard geometric constraints to guide and modulate the diffusion process for three-dimensional crystal geometries, thereby rectifying the denoising trajectory, confining the generative process to a physically valid manifold, guaranteeing both structural plausibility and computational precision. As a result, this leads to a significant enhancement in the stability, uniqueness, and novelty (SUN) [14] of the predicted materials, as well as the matching rate metrics [19].

Below, we outline the core methodology, with full implementation details, as well as training and testing configurations provided in Appendix A and B, respectively.

First, we use two large language models (LLMs) to directly infer fine-grained crystallographic symmetry from compositional inputs. Both models are built upon the Transformer architecture [22], and we replace the standard feed-forward networks within each Transformer block with soft mixture-of-experts (SoftMoE) layers [23] to enhance model capacity. This design enables multiple experts to specialize in distinct compositional patterns, substantially boosting model capacity without a commensurate rise in computational cost, as only a small, softly weighted subset of experts is activated at each position.

The first LLM, denoted as LLM_g, takes as input an atomic sequence representation of the composition, expanded to explicitly reflect the atom counts N in the unit cell, and outputs a probability distribution over the 230 crystallographic space groups:

$$\begin{aligned} &S_g = \arg\max_i p_g(i|C_{\text{atoms}}), \\ &p_g(i|C_{\text{atoms}}) = LLM_g(C_{\text{atoms}}), \\ &1 \le i \le 230, \end{aligned} \tag{1}$$

where $C_{\text{atoms}} = [A, A, A, \dots, B, B, B, B, B, \dots, C, C, \dots]$ is the expanded atomic sequence for elements $A, B, C, \dots$ derived from the given composition, proportionally expanded to match the number of atoms in the unit cell; $p_g[i]$ is the predicted probability that the crystal belongs to the i-th space group; S_g represents the predicted space group.

The second LLM, denoted as LLM_w, takes the same expanded atomic sequence together with the predicted space group S_g and outputs a probability distribution over Wyckoff letters compatible with that space group for each atom. Rather than concatenating S_g naively to the input, we encode the predicted space group into a continuous embedding and inject it into each transformer block via the feature-wise linear modulation (FiLM) [24] module. This FiLM-based conditioning ensures that Wyckoff letter predictions are explicitly modulated by the inferred space group, rather than being learned in an implicitly entangled fashion. Concretely, FiLM(S_g) produces per-channel scaling and shifting coefficients that modulate the intermediate representations of LLM_w, allowing the model to adapt its representation to the symmetry class:

$$\begin{aligned} &p_w(l_n = l|C_{\text{atoms}}) = LLM_w\big(C_{\text{atoms}}, \text{FiLM}(S_g)\big), \\ &l_n \in L(S_g), \quad 1 \le n \le N, \end{aligned} \tag{2}$$

where $p_w(l_n = l|C_{\text{atoms}})$ denotes the probability that the n-th atom is assigned to letter l, $L(S_g)$ is the set of admissible Wyckoff letters for space group S_g. Specific details regarding the network architectures and hyperparameter configurations of these two large language models are provided in Appendix A.1-A.2 and B.

Second, we formulate the Wyckoff letter assignment for each atom as a constrained optimization problem based on the probability distribution $p_w(l_n|C_{\text{atoms}})$ predicted by the LLM, and propose an efficient algorithm to solve it. This formulation strictly adheres to the combinatorial constraints imposed by the Wyckoff site multiplicity rules under the inferred space group symmetry. Specifically, the constrained maximization objective is defined as follows:

$$\begin{aligned} \{l_n^*\}_{n=1}^N = \arg\max_{\{l_n\}_{n=1}^N} \quad & \sum_{n=1}^N \log p_w(l_n|C_{\text{atoms}}), \\ s.t.\ \ & l_n \in L(S_g), \\ & \text{Count}_e(l_n) \bmod \text{mult}(l_n) = 0, \\ & \sum_{l \in L(S_g)} \text{Count}_e(l) = N_e, \\ & \forall\, e \in \mathcal{E} = \{A, B, C, \dots\}, \end{aligned} \tag{3}$$

where $\text{mult}(l_n)$ refers to the multiplicity of Wyckoff letter l_n, and $\text{Count}_e(l_n)$ is the number of atoms of element e assigned to l_n, N_e is the number of atoms of element e in a cell, the set $\{l_n^*\}_{n=1}^N$ represents the optimal Wyckoff letter assignment. The key point here is that $\text{Count}_e(l_n)$ must be an integer multiple of $\text{mult}(l_n)$, a hard constraint that cannot be satisfied by simply using the maximum probability outputs of each token from the LLM. Fundamentally, deriving the exact global optimum under these precise constraints constitutes an NP-hard combinatorial optimization problem. Consequently, finding the solution for Eq. (3) via brute-force enumeration is computationally intractable, as the search space grows exponentially with the number of atoms, scaling

as $O(|L(S_g)|^N)$. To overcome this bottleneck, we employ propose a beam search algorithm to efficiently solve the optimization problem. By maintaining only the most promising candidates within a fixed beam width, this strategy drastically compresses the time complexity from exponential to a linear $O(N)$, rendering the prediction of physically valid Wyckoff assignments computationally tractable. Comprehensive details regarding this algorithm are provided in Appendix A.3.

To generate the 20 candidates for each test composition, we employ a hierarchical sampling strategy to ensure both macroscopic and microscopic structural diversity. First, we select the Top-5 most probable space groups predicted by LLM_g. Subsequently, for each selected space group, we extract the Top-4 valid Wyckoff assignments using our constrained beam search algorithm. This combination yields exactly 20 distinct symmetry templates per composition, which are then used to guide the diffusion generation process.

Third, we guide and constrain the diffusion-based generation of 3D atomic structures using the predicted space group and Wyckoff site template. To instantiate this approach, we adopt the graph neural network (GNN) applied by DiffCSP++[10] as the backbone network of diffusion model, effectively repurposing its exploration to strictly adhere to the symmetry constraints inferred by our method. Specifically, we employ a joint-rectification mechanism on both lattice and fractional coordinates. For the lattice, we constrain its $O(3)$-invariant logarithmic parameterization by applying a binary mask dictated by the inferred crystal family, ensuring the unit cell geometry strictly adheres to the specific constraints on lattice lengths and inter-axial angles defined by the crystal family. Simultaneously, for the fractional coordinates $\mathbf{F}_t$, we employ a subspace projection and reconstruction mechanism, effectively rectifying any symmetry violations in each denoising state of fractional coordinates, ensuring that the generated crystal structure strictly resides on the geometric manifold defined by the target Wyckoff templates. Further details regarding the lattice masking and coordinate reconstruction are available in Appendix A.4.

To evaluate our approach, we benchmark it against a comprehensive suite of generative models. We adopt DiffCSP++ [10] as the primary baseline, as it represents the current state-of-the-art (SOTA) for standard CSP and serves as the most stringent benchmark for composition-conditioned structural generation. To provide a broader context for structural reconstruction fidelity, we also encompass CDVAE [18], DiffCSP [19], and CrystaLLM [9] in our comparative analysis, specifically regarding the Matching Rate metric. While MatterGen [14] and CrystalFormer [20] are also leading methods in materials generation, they are excluded from direct comparison due to a fundamental discrepancy in task formulation. They employ a joint generation paradigm that co-samples chemical composition and structural coordinates. While this enables broad exploration of the joint space of compositions and structures, it lacks the strict conditionality inherent to CSP, where the core objective is to resolve the atomic structure for a fixed, pre-specified composition. Thus, a direct quantitative comparison is omitted.

To provide a comprehensive evaluation of our model, we adopt the Top-20 SUN (stability, uniqueness, and novelty) metrics based on the core principles of [14], alongside the Top-20 Matching Rate [19]. The detailed definitions and adapted calculation protocols for these metrics, designed to accommodate our extensive Top-20 evaluation setting, are provided in Appendices C.1 and C.2. The SUN metrics emphasize physical plausibility, structural diversity, and originality, aspects that are more directly aligned with the objectives of open-ended discovery in materials science; while the Matching Rate prioritizes structural fidelity by quantifying the precision with which the model reconstructs the experimental ground-truth (GT) geometry within defined coordinate and symmetry tolerances. It is worth noting that, these two metrics can be inherently contradictory in a Top-1 evaluation because a model must choose between replicating a known structure to achieve a high Matching Rate or exploring a previously unknown one to achieve high Novelty. This tension is effectively resolved in our Top-20 setting. By generating multiple candidates for each composition, the model is afforded the capacity to simultaneously demonstrate structural fidelity by recovering the experimental ground truth and chemical creativity by proposing stable, novel phases. Thus, reporting both metrics at Top-20 provides a holistic assessment of the model's dual role as both a precise structural reconstructor and a robust discovery engine for uncharted materials space.

All experiments are conducted on three standard CSP benchmark datasets: Perov-5 [25], MP-20 [26], and MPTS-52 [10]. These datasets were previously used in DiffCSP++ and are employed here with identical training, validation and testing splits to ensure a fair comparison. Detailed descriptions and statistical information regarding these three datasets are available in Appendix C.2. The experimental results for the DiffCSP++ baseline are obtained using its official open-source scripts for standard training and inference [27]. Table I presents a side-by-side comparison between the performance of this original method and that of our symmetry-enhanced method.

As shown in Table I, our method yields notable and consistent improvements over DiffCSP++ across all three benchmarks on the comprehensive SUN metrics. On the MP-20 dataset, our method improves stability and novelty by approximately 124% and 71% respectively relative to the baseline. The advantages are even more pronounced on the challenging MPTS-52 dataset, where our method achieves a relative gain of about 255% in stabil-

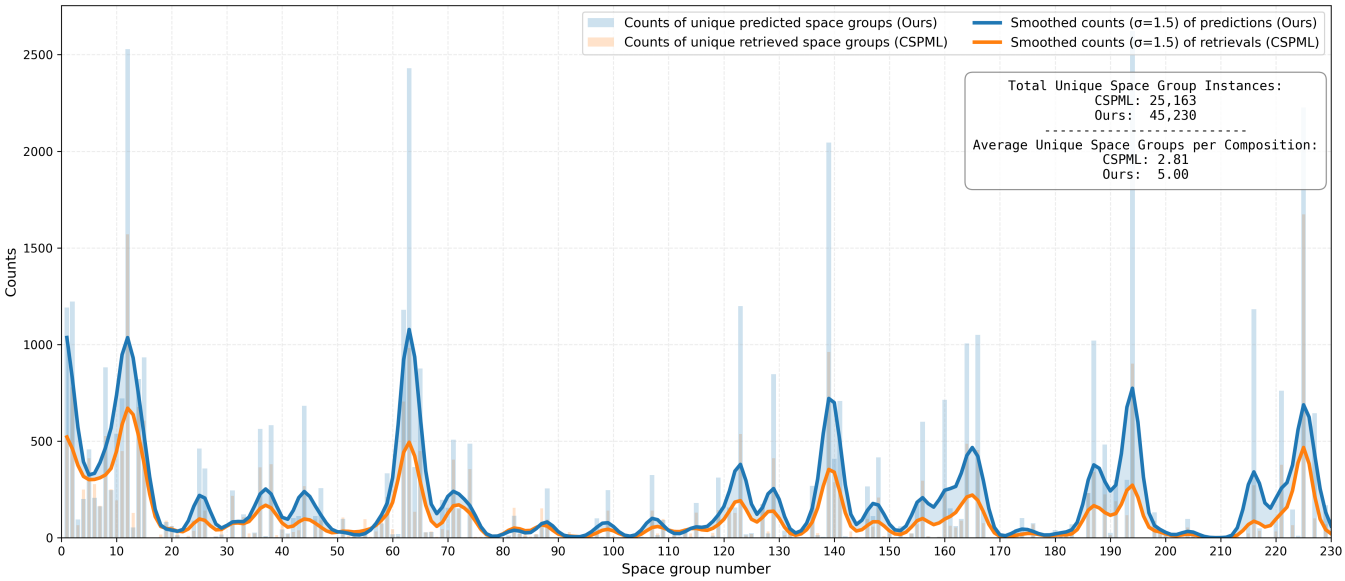

FIG. 2: Absolute frequency distribution (raw counts) of space groups among the candidates across the testing set of MP-20. Counts are calculated using a unique-counting principle per composition, where any specific space group present in the candidate structures for a single testing composition is counted exactly once. Our generative approach yields a profoundly larger total unique count, demonstrating a consistently higher richness in symmetry exploration per composition compared to the localized redundancy of the retrieval baseline, i.e. CSPML [21].

TABLE I: Comparison of Top-20 SUN metrics (%) across three benchmarks. Results for DiffCSP++ [10] are reproduced using the official source code implementation [27], utilizing the CSPML [21] retrieval method to obtain space group templates as described in the original study.

Dataset	Method	Stability	Uniqueness	Novelty	**SUN**
MP-20	DiffCSP++	36.51	**100.0**	54.82	14.55
	Ours	**81.79**	**100.0**	**93.67**	**35.58**
Perov-5	DiffCSP++	75.77	**100.0**	99.52	73.39
	Ours	**94.98**	**100.0**	**99.67**	**92.42**
MPTS-52	DiffCSP++	11.95	**100.0**	45.97	5.44
	Ours	**42.43**	**100.0**	**70.53**	**25.94**

TABLE II: Comparison of Top-20 Matching Rates (%) across three benchmarks. Experimental results for CDVAE [18], DiffCSP [19], and CrystaLLM [9] are taken from Antunes *et al.* [9]. Results for DiffCSP++ [10] are reproduced from the official source code [27] using the CSPML [21] retrieval-based template method as described in the original study.

Dataset	Method	Matching Rate
MP-20	CDVAE	66.95
	DiffCSP	77.93
	CrystaLLM	73.97
	DiffCSP++	74.65
	Ours	**81.70**
Perov-5	CDVAE	88.51
	DiffCSP	98.60
	CrystaLLM	97.60
	DiffCSP++	99.84
	Ours	**99.95**
MPTS-52	CDVAE	20.79
	DiffCSP	34.02
	CrystaLLM	33.75
	DiffCSP++	40.53
	Ours	**43.26**

ity and 53% in novelty. Crucially, these component-level improvements compound to yield a striking 376% increase in the overall SUN metric. Even on Perov-5, which features relatively simple structural motifs, our method maintains a clear advantage in stability while matching the saturated uniqueness and novelty scores of the baseline. The significant rise in the overall SUN metric across all benchmark datasets confirms that our method generates candidates that are simultaneously more physically stable and structurally novel, while preserving the high standards of uniqueness.

As case studies, Figs. 3 and 4 visualize the prediction results for two representative testing samples: Zr_3Fe_8Mo and $NaCr_4O_8$. These examples expose an inherent generative dilemma in the retrieval-based DiffCSP++ baseline: its predicted structures systematically fail either the novelty or stability criteria. For Zr_3Fe_8Mo, the baseline

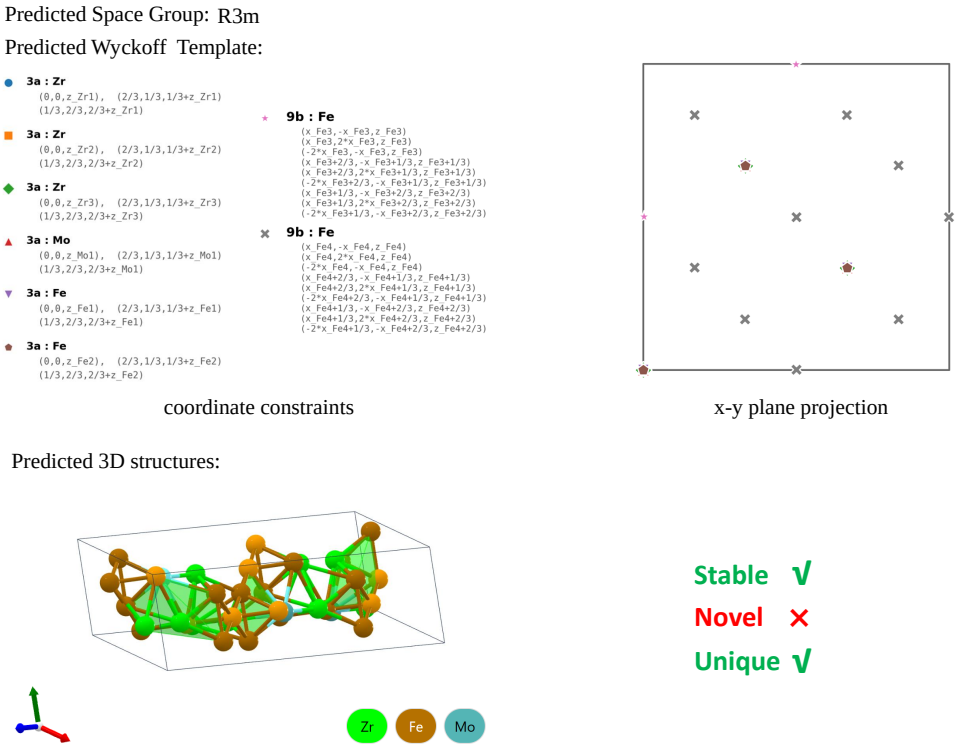

(a) Retrieved and prediction results of DiffCSP++.

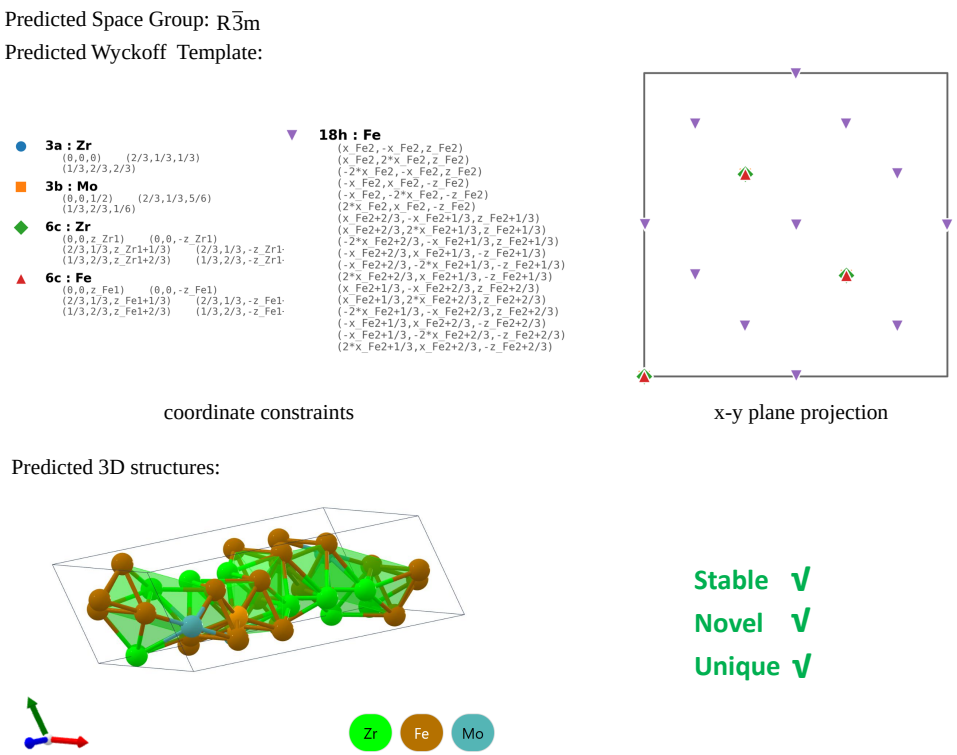

(b) Prediction results of our method.

FIG. 3: Visual comparison of prediction results from DiffCSP++ and our method for a testing sample, i.e., Zr_3Fe_8Mo ($N = 36$). The definition for stability, uniqueness, and novelty are detailed in Appendix C.1.

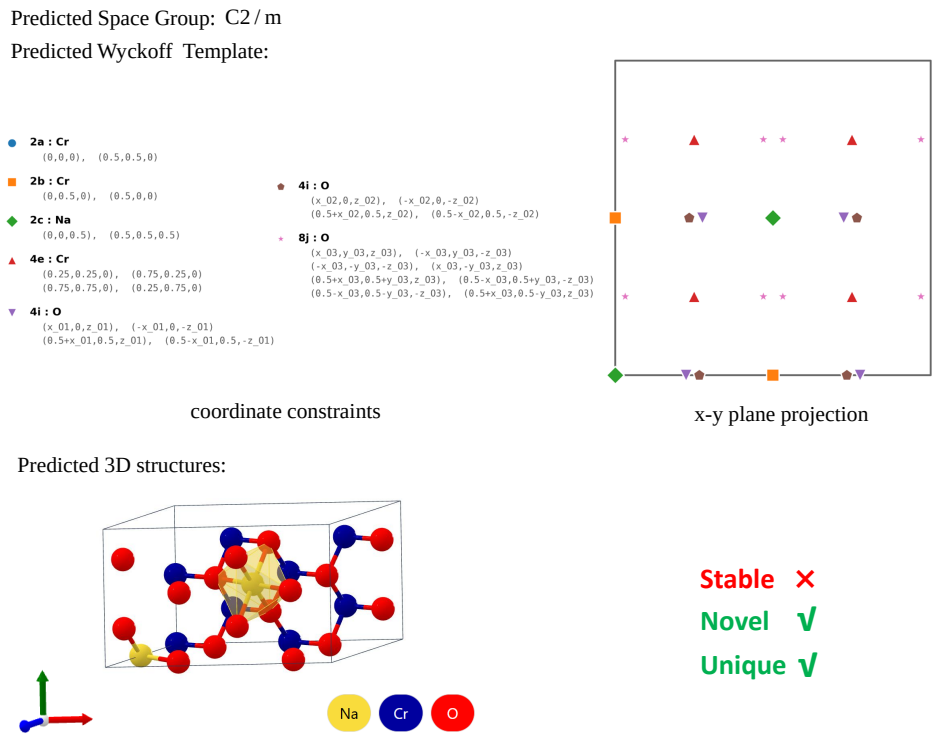

(a) Retrieved and prediction results of DiffCSP++.

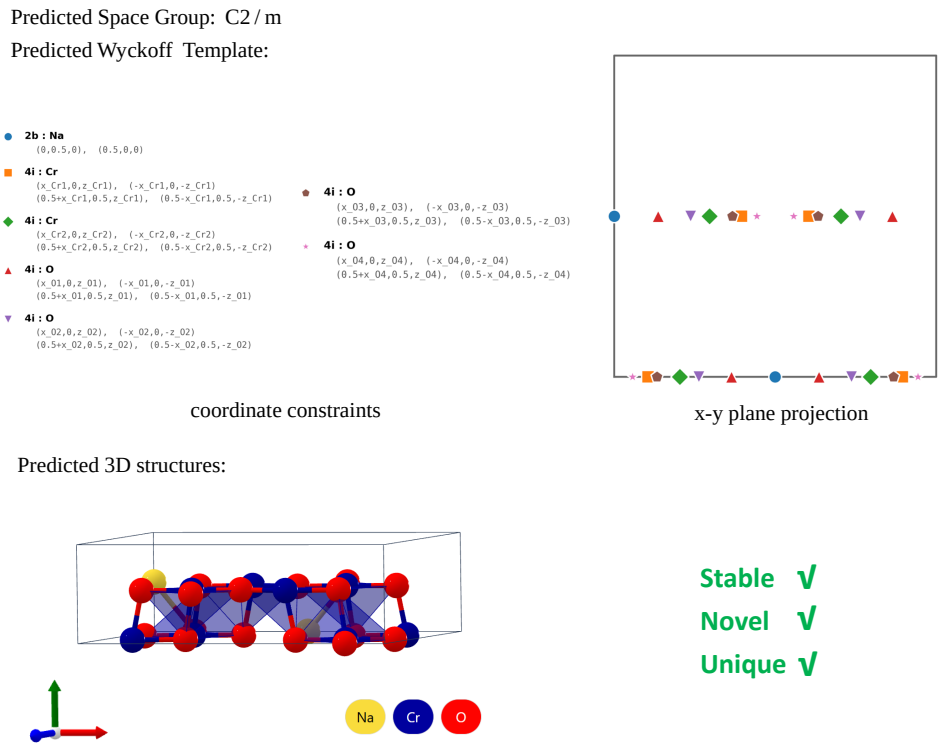

(b) Prediction results of our method.

FIG. 4: Visual comparison of prediction results from DiffCSP++ and our method for a testing sample, i.e., $NaCr_4O_8$ ($N = 26$). The definition for stability, uniqueness, and novelty are detailed in Appendix C.1.

merely retrieves an exact match of a documented non-centrosymmetric $R3m$ phase, which guarantees stability but completely fails the novelty criterion. Furthermore, it forces the 36 atoms into a fragmented, lower-symmetry template comprising multiple $3a$ and $9b$ orbits. In contrast, our symmetry-driven approach bypasses empirical retrieval to discover a genuinely novel centrosymmetric phase under the higher-symmetry $R\bar{3}m$ space group by elegantly allocating the atoms to higher-multiplicity orbits such as $18h$ and $6c$. Conversely, the baseline's prediction for $NaCr_4O_8$ is novel but highly unstable because it rigidly assigns the framework-forming Cr atoms to zero-degree-of-freedom (0-DOF) special sites ($2a$, $2b$, and $4e$) under the $C2/m$ space group. This mathematically locks the coordinates, preventing local relaxation and inducing severe microscopic strain within the Cr–O octahedral network. Our method elegantly resolves this by allocating the Cr atoms to distinct $4i$ orbits, whose two internal degrees of freedom (x and z) provide the critical geometric flexibility to adaptively optimize bond lengths and navigate toward a thermodynamically stable local minimum. Ultimately, by inferring compatible space groups and Wyckoff assignments directly from the stoichiometry, our approach effectively overcomes these generative bottlenecks to yield candidate materials that successfully satisfy all three criteria: stability, uniqueness, and novelty.

The performance disparity observed in Table I and Fig. 3 – 4 stem from the fundamental transition from retrieval-based memorization to generative reasoning. The baseline relies on CSPML, which essentially operates as a static lookup system. It rests on the isomorphism assumption, presupposing that for any new material, a structurally identical twin already exists in the training database. Consequently, this approach fails in data-sparse regimes or when exploring truly novel materials where no such prototype exists. When the model forces a new querying composition into a retrieved but topologically mismatched template, it introduces geometric frustration. The atoms are coerced into energetically unfavorable coordination environments to satisfy incorrect symmetry constraints, directly leading to poor stability. This reliance on data lookup inherently confines the model to the known structural motifs, rendering it incapable of discovering new polymorphs that lie outside the existing library.

In stark contrast, our method reformulates symmetry determination as *ab initio* generative inference coupled with rigorous constrained optimization. Instead of retrieving existing solutions, the model learns a unified representation space from diverse structural data, enabling it to generalize and derive valid Wyckoff patterns for unseen compositions based on chemical rules. Crucially, a heuristic combinatorial optimization algorithm enforces algebraic consistency, ensuring the sum of site multiplicities matches the atomic stoichiometry. This mechanism empowers the model to explore uncharted chemical space while confining stochastic diffusion to a symmetry-compliant configurational space, guaranteeing output rationality. By eliminating symmetry-breaking artifacts of unconstrained generation, our framework enables inverse design of materials with high structural novelty and strict physical rigor.

To further quantify generative symmetry diversity, we evaluate the distribution of unique space group instances generated across the testing set, as shown in Fig. 2. To faithfully capture the true exploratory richness for each individual composition, we apply a strict unique-counting principle: a unique space group instance is defined such that if a specific space group appears within the candidate structures generated for a single testing composition, it is counted exactly once for that composition, regardless of its redundancy. The results demonstrate that the CSPML retrieval baseline [21] often collapses into retrieving multiple structural templates that share the identical space group for a given composition. Because of this localized redundancy, multiple retrieved candidates frequently contribute only a single unique space group count, which drastically shrinks its total aggregate score. In contrast, our generative approach explicitly infers multiple mutually distinct space groups directly from the probability distribution predicted by the language models. This mechanism yields a profoundly larger total count of unique instances and demonstrates a consistently richer and more abundant exploration across different space groups for each of the composition, as evidenced by the higher frequency observed across nearly all space group indices in Fig. 2.

Complementing the discovery-oriented SUN metrics, Table II presents the Top-20 Matching Rate, which quantifies the model's ability to reconstruct experimentally known ground-truth structures. As shown, our method consistently achieves state-of-the-art performance across all three benchmarks, outperforming all of the baseline methods. This result is scientifically significant when interpreted in the context of generative design. In *ab initio* materials discovery, the Matching Rate confirms that the model's generative distribution covers the manifold of physically realized structures. A high Matching Rate indicates that the symmetry constraints imposed by our framework do not overly restrict the search space or exclude valid ground-truth configurations. Instead, they effectively guide the diffusion process within a chemically reasonable manifold. Consequently, the combination of superior SUN scores (Table I) and leading Matching Rates (Table II) demonstrates that our method resolves the trade-off between exploration and exploitation: it is robust enough to recover known stable phases with high fidelity while possessing the generative flexibility to propose novel, stable polymorphs beyond the existing samples.

In summary, this work presents a symmetry-driven

CSP framework that advances beyond conventional paradigm. By reducing reliance on pre-existing prototypes, leveraging chemical rules, and enforcing strict algebraic consistency and symmetry compliance through an efficient generative framework incorporating probability distribution predictions from large language models and an efficient heuristic search, it renders an inherently NP-hard combinatorial optimization problem computationally tractable. Consequently, it delivers robust performance in data-sparse regimes and novel material exploration. Experimental results show significant gains over state-of-the-art methods across comprehensive SUN metrics, transcending known structural motifs, as well as superior matching rates. This framework establishes a reliable, highly exploratory pathway for advanced functional material inverse design, redefining CSP from retrieval-based memorization to constrained *ab initio* generative inference.

This work was supported by the Advanced Materials–National Science and Technology Major Project (Grant No. 2025ZD0618401), the National Natural Science Foundation of China (Grant No. 12134012), the Strategic Priority Research Program of the Chinese Academy of Sciences (Grant No. XDB0500201). The numerical calculations were performed on the USTC High-Performance Computing facilities and Hefei advanced computing center.

* Shi Yin and Jinming Mu contributed equally to this work. †Shi Yin (shiyin@iai.ustc.edu.cn) and Linxin He (helx@ustc.edu.cn) are the corresponding authors.

[1] M. A. Green, A. Ho-Baillie, and H. J. Snaith, The emergence of perovskite solar cells, Nature photonics **8**, 506 (2014).

[2] L. I. Berger, *Semiconductor materials* (CRC press, 2020).

[3] Q. Jiang and K. Zhu, Rapid advances enabling high-performance inverted perovskite solar cells, Nature Reviews Materials **9**, 399 (2024).

[4] J. Ding, D. Ji, Y. Yue, and M. M. Smedskjaer, Amorphous materials for lithium-ion and post-lithium-ion batteries, Small **20**, 2304270 (2024).

[5] R. Langer and D. A. Tirrell, Designing materials for biology and medicine, Nature **428**, 487 (2004).

[6] Z. W. Seh, J. Kibsgaard, C. F. Dickens, I. Chorkendorff, J. K. Nørskov, and T. F. Jaramillo, Combining theory and experiment in electrocatalysis: Insights into materials design, Science **355**, eaad4998 (2017).

[7] N. Marzari, A. Ferretti, and C. Wolverton, Electronic-structure methods for materials design, Nature materials **20**, 736 (2021).

[8] R. Jiao, W. Huang, P. Lin, J. Han, P. Chen, Y. Lu, and Y. Liu, Crystal structure prediction by joint equivariant diffusion on lattices and fractional coordinates, in *Workshops of the Eleventh International Conference on Learning Representations* (2023).

[9] L. M. Antunes, K. T. Butler, and R. Grau-Crespo, Crystal structure generation with autoregressive large language modeling, Nature Communications (2024).

[10] R. Jiao, W. Huang, Y. Liu, D. Zhao, and Y. Liu, Space group constrained crystal generation, in *The Twelfth International Conference on Learning Representations* (2024).

[11] S. Yang, S. Batzner, R. Gao, M. Aykol, A. Gaunt, B. McMorrow, D. Rezende, D. Schuurmans, I. Mordatch, and E. D. Cubuk, Generative hierarchical materials search, in *Advances in Neural Information Processing Systems* (2024) pp. 38799–38819.

[12] R. Zhu, W. Nong, S. Yamazaki, and K. Hippalgaonkar, Wycryst: Wyckoff inorganic crystal generator framework, Matter **7**, 3469 (2024).

[13] Y. Han, C. Ding, J. Wang, H. Gao, J. Shi, S. Yu, Q. Jia, S. Pan, and J. Sun, Efficient crystal structure prediction based on the symmetry principle, Nature Computational Science (2025).

[14] C. Zeni, R. Pinsler, D. Zügner, A. Fowler, M. Horton, X. Fu, Z. Wang, A. Shysheya, J. Crabbé, S. Ueda, *et al.*, A generative model for inorganic materials design, Nature (2025).

[15] J. Xu, X. Wang, W. Cheng, Y.-P. Cao, Y. Shan, X. Qie, and S. Gao, Dream3d: Zero-shot text-to-3d synthesis using 3d shape prior and text-to-image diffusion models, in *Proceedings of the IEEE/CVF Conference on Computer Vision and Pattern Recognition* (2023) pp. 20908–20918.

[16] C. Wang, H.-Y. Peng, Y.-T. Liu, J. Gu, and S.-M. Hu, Diffusion models for 3d generation: A survey, Computational Visual Media **11**, 1 (2025).

[17] Y. Xin, Z. Xie, Y. Chen, P. Gao, H. J. Zhao, J. Lv, Y. Wang, and Y. Ma, Symmetry-oriented enumeration method for molecular crystal structure prediction and its application, Physical Review B **111**, 134112 (2025).

[18] T. Xie, X. Fu, O. Ganea, R. Barzilay, and T. S. Jaakkola, Crystal diffusion variational autoencoder for periodic material generation, in *The Tenth International Conference on Learning Representations* (2022).

[19] R. Jiao, W. Huang, P. Lin, J. Han, P. Chen, Y. Lu, and Y. Liu, Crystal structure prediction by joint equivariant diffusion, in *Advances in Neural Information Processing Systems 36: Annual Conference on Neural Information Processing Systems 2023* (2023).

[20] Z. Cao, X. Luo, J. Lv, and L. Wang, Space group informed transformer for crystalline materials generation, Science Bulletin (2025).

[21] M. Kusaba, C. Liu, and R. Yoshida, Crystal structure prediction with machine learning-based element substitution, Computational Materials Science **211**, 111496 (2022).

[22] A. Vaswani, N. Shazeer, N. Parmar, J. Uszkoreit, L. Jones, A. N. Gomez, L. Kaiser, and I. Polosukhin, Attention is all you need, in *Conference on Neural Information Processing Systems* (2017) pp. 5998–6008.

[23] J. Puigcerver, C. R. Ruiz, B. Mustafa, and N. Houlsby, From sparse to soft mixtures of experts, in *The Twelfth International Conference on Learning Representations* (2024).

[24] E. Perez, F. Strub, H. De Vries, V. Dumoulin, and A. Courville, Film: Visual reasoning with a general conditioning layer, in *Proceedings of the AAAI conference on artificial intelligence* (2018).

[25] I. E. Castelli, D. D. Landis, K. S. Thygesen, S. Dahl, I. Chorkendorff, T. F. Jaramillo, and K. W. Jacobsen, New cubic perovskites for one-and two-photon water

splitting using the computational materials repository, Energy & Environmental Science **5**, 9034 (2012).
[26] A. Jain, S. P. Ong, G. Hautier, W. Chen, W. D. Richards, S. Dacek, S. Cholia, D. Gunter, D. Skinner, G. Ceder, *et al.*, Commentary: The materials project: A materials genome approach to accelerating materials innovation, APL materials **1**, 011002 (2013).
[27] `https://github.com/jiaor17/DiffCSP-PP`.
[28] J. Su, M. H. M. Ahmed, Y. Lu, S. Pan, W. Bo, and Y. Liu, Roformer: Enhanced transformer with rotary position embedding, Neurocomputing **568**, 127063 (2024).
[29] H. Yang, C. Hu, Y. Zhou, X. Liu, Y. Shi, J. Li, G. Li, Z. Chen, S. Chen, C. Zeni, *et al.*, Mattersim: A deep learning atomistic model across elements, temperatures and pressures, arXiv preprint arXiv:2405.04967 (2024).
[30] S. P. Ong, W. D. Richards, A. Jain, G. Hautier, M. Kocher, S. Cholia, D. Gunter, V. L. Chevrier, K. A. Persson, and G. Ceder, Python materials genomics (pymatgen): A robust, open-source python library for materials analysis, Computational Materials Science **68**, 314 (2013).
[31] J. Schmidt, N. Hoffmann, H.-C. Wang, P. Borlido, P. J. Carriço, T. F. Cerqueira, S. Botti, and M. A. Marques, Large-scale machine-learning-assisted exploration of the whole materials space, arXiv preprint arXiv:2210.00579 (2022).

Appendix A: Detailed Design on Model Architectures and Algorithms

A.1. Input Featurization and Embeddings

As defined in the main text, the input to our language models is the expanded atomic sequence C_{atoms}. For the n-th atom in this sequence (where $1 \leq n \leq N$), let v_n denote its corresponding token index in the vocabulary. To capture the rich chemical semantics required for crystallographic reasoning, we construct a composite input representation $\mathbf{x}_n$ by fusing the learnable token embedding with explicit physicochemical features derived from the periodic table.

Token Embeddings. We utilize a learnable lookup table $\mathbf{E}_{tok} \in \mathbb{R}^{V \times D}$ to map the discrete index v_n of each semantic token (e.g. the element type) to a dense semantic vector $\mathbf{h}_n$:

$$\mathbf{h}_n = \mathbf{E}_{tok}[v_n] \in \mathbb{R}^D. \tag{A1}$$

Physicochemical Features. Simultaneously, for the n-th atom, we retrieve its explicit chemical attributes: the atomic number Z_n, the group number G_n, and the period number P_n. To effectively integrate this discrete information, we employ three separate embedding layers $(\mathbf{E}_Z, \mathbf{E}_G, \mathbf{E}_P)$ to project these attributes into the latent space. The projected features are concatenated and fused via a multi-layer perceptron (MLP) to form the chemical feature vector $\mathbf{f}_n \in \mathbb{R}^D$:

$$\mathbf{f}_n = \text{MLP}\left(\mathbf{E}_Z[Z_n] \oplus \mathbf{E}_G[G_n] \oplus \mathbf{E}_P[P_n]\right), \tag{A2}$$

where $\oplus$ denotes the concatenation operation.

Final Input Representation. The final input embedding $\mathbf{x}_n$ passed to the first transformer layer is the element-wise sum of the token embedding and the chemical feature vector, ensuring that both identity and periodicity information are preserved:

$$\mathbf{x}_n = \mathbf{h}_n + \mathbf{f}_n. \tag{A3}$$

Symmetry Conditioning. For the symmetry-conditioned model LLM_w, the space group label S_g predicted by LLM_g is explicitly embedded to serve as the global context. We use a dedicated embedding layer $\mathbf{E}_{sg}$ to map S_g to a continuous vector $\mathbf{e}_{sg}$:

$$\mathbf{e}_{sg} = \mathbf{E}_{sg}[S_g] \in \mathbb{R}^D. \tag{A4}$$

This vector $\mathbf{e}_{sg}$ is subsequently used to generate the modulation parameters for the FiLM layers in the Transformer blocks.

A.2. Transformer Block with SoftMoE and FiLM

Both LLM_g and LLM_w rely on a unified modified Transformer architecture. To handle the complex mapping between composition and symmetry, we replace the standard Feed-Forward Network (FFN) with Soft Mixture-of-Experts (SoftMoE) layers in both models to enhance capacity without increasing inference cost. In the following formulation, we detail the architecture of the more complex LLM_w, which explicitly incorporates symmetry conditioning. It is important to note that LLM_g shares an similar structural backbone, including the Multi-head attention module and the SoftMoE mechanism, but omits the Feature-wise Linear Modulation (FiLM) modules, as it operates without prior symmetry conditions.

Multi-Head Attention with RoPE and FiLM. Let $\mathbf{X}$ be the input to the attention block. We first apply LayerNorm to obtain $\mathbf{Y} = \text{LayerNorm}(\mathbf{X})$. To implement multi-head attention with H heads, the input is projected into H distinct subspaces. For each head $h \in \{1, \ldots, H\}$, the Queries, Keys, and Values are computed as:

$$\mathbf{Q}_h = \mathbf{W}_Q^h \cdot \mathbf{Y}, \quad \mathbf{K}_h = \mathbf{W}_K^h \cdot \mathbf{Y}, \quad \mathbf{V}_h = \mathbf{W}_V^h \cdot \mathbf{Y}. \tag{A5}$$

Rotary Positional Embeddings (RoPE) [28] are applied to each $\mathbf{Q}_h$ and $\mathbf{K}_h$ to encode relative positions. The attention output for the h-th head, denoted as $\mathbf{A}_h$, is computed via softmax, and the final output $\mathbf{O}$ is obtained by concatenating all heads and applying a linear projection:

$$\begin{aligned} \mathbf{A}_h &= \text{softmax}\left(\frac{\mathbf{Q}_h \cdot \mathbf{K}_h^\top}{\sqrt{d_k}}\right) \cdot \mathbf{V}_h, \\ \mathbf{O} &= \text{Concat}(\mathbf{A}_1, \ldots, \mathbf{A}_H) \cdot \mathbf{W}_O. \end{aligned} \tag{A6}$$

In LLM_w, this output is modulated by the space group embedding $\mathbf{e}_{sg}$ via Feature-wise Linear Modulation (FiLM). The modulation parameters $(\boldsymbol{\gamma}, \boldsymbol{\beta})$ are derived from $\mathbf{e}_{sg}$:

$$(\boldsymbol{\gamma}, \boldsymbol{\beta}) = \mathrm{MLP}(\mathbf{e}_{sg}), \quad \mathrm{FiLM}(\mathbf{O}) = \mathbf{O} \odot (1+\boldsymbol{\gamma}) + \boldsymbol{\beta}, \tag{A7}$$

where $\cdot$ denotes matrix multiplication and $\odot$ denotes element-wise multiplication.

SoftMoE Layer with FiLM. The intermediate representation is passed to the SoftMoE layer. Let $\mathbf{Y}$ denote the normalized input to this block. We compute the expert dispatch weights by mapping the input to expert scores $\mathbf{W}_r\mathbf{Y}$. For each token n, we select the top-k experts T_n. The routing weights $g_{n,e}$ for the e-th expert and n-th token are normalized within the selected set:

$$\begin{aligned} \mathbf{P} &= \mathrm{softmax}(\mathbf{W}_r\mathbf{Y}), \\ g_{n,e} &= \frac{P_{n,e}}{\sum_{j \in T_n} P_{n,j}} \cdot \mathbb{I}[e \in T_n]. \end{aligned} \tag{A8}$$

Here, $\mathbb{I}[e \in T_n]$ denotes the indicator function, taking value 1 if expert e is in T_n, and 0 otherwise.

The output $\mathbf{Y}_{out}$ aggregates the processed features from all experts:

$$\mathbf{Y}_{out} = \sum_{e=1}^{E} \mathrm{Scatter}\left(n, g_{n,e} \cdot \mathrm{FFN}_e(\mathbf{Y}_n)\right). \tag{A9}$$

Similar to the attention block, the output of the SoftMoE layer in LLM_w is modulated by the space group context:

$$\begin{aligned} (\boldsymbol{\gamma}', \boldsymbol{\beta}') &= \mathrm{MLP}(\mathbf{e}_{sg}), \\ \mathrm{FiLM}(\mathbf{Y}_{out}) &= \mathbf{Y}_{out} \odot (1 + \boldsymbol{\gamma}') + \boldsymbol{\beta}'. \end{aligned} \tag{A10}$$

A.3. Constrained Beam Search Algorithm

Search State Definition. Let the input atomic sequence be denoted by $C_{\text{atoms}} = [A, A, A, \ldots, B, B, B, B, B, \ldots, C, C, \ldots]$, as defined in the main text. We define $\mathcal{E} = \{A, B, C, \ldots\}$ as the set of unique element types present in C_{atoms}. A hypothesis at step n is formally defined as a tuple $h_n = (\mathbf{l}_{1:n}, s_{1:n}, \mathbf{Count}_{1:n})$, where:

- $\mathbf{l}_{1:n} = [l_1, \ldots, l_n]$ is the partial sequence of assigned Wyckoff letters up to atom n.
- $s_{1:n} = \sum_{i=1}^{n} \log p_w(l_i | C_{\text{atoms}})$ is the cumulative log-probability score of the assignment sequence.
- $\mathbf{Count}_{1:n} \in \mathbb{N}^{|\mathcal{E}| \times |L(S_g)|}$ is the global counter matrix. The entry $\mathbf{Count}_{1:n}[e, l]$ records the number of atoms of element type $e \in \mathcal{E}$ that have been assigned to Wyckoff letter l within the partial sequence $\mathbf{l}_{1:n}$. This matrix allows for the independent verification of multiplicity constraints for each element type.

Expansion and Pruning. At step n, let the current atom be $e_n = C_{\text{atoms}}[n]$. We consider assigning a letter $l \in L(S_g)$. To accelerate the search, candidate letters are evaluated in descending order of their probability $p_w(l_n = l | C_{\text{atoms}})$. We enforce the algebraic consistency constraint via an *early pruning* check: a branch is valid if and only if the current count $\mathbf{Count}_{1:n}[e_n, l]$ plus the number of remaining atoms of element e_n in the sequence is sufficient to reach the next integer multiple of $\mathrm{mult}(l)$. Branches failing this check are discarded immediately.

The complete procedure is detailed in Algorithm 1.

A.4. Diffusion Rectification via Predicted Symmetry

Once the optimal space group S_g and the atom-wise Wyckoff assignment $\mathbf{l}^* = \{l_1^*, \ldots, l_N^*\}$ are determined, we utilize them to rectify the intermediate states of the diffusion process. This rectification is applied at each denoising step t to explicitly enforce symmetry constraints on the lattice and fractional coordinates.

Lattice Rectification. The lattice matrix $\mathbf{L}_t$ is parameterized by a coefficient vector $\mathbf{k}_t \in \mathbb{R}^6$ in the $O(3)$-invariant logarithmic space [10]. The inferred space group S_g imposes hard constraints on specific dimensions of $\mathbf{k}_t$. By enforcing these constraints, we ensure that the resulting lattice vectors strictly adhere to the specific edge lengths and angular relationships mandated by the crystal system. Let $\mathbf{m}_{S_g} \in \{0, 1\}^6$ be the binary mask where 0 indicates a constrained dimension. We rectify the lattice state via:

$$\hat{\mathbf{k}}_t = \mathbf{m}_{S_g} \odot \mathbf{k}_t + (\mathbf{1} - \mathbf{m}_{S_g}) \odot \mathbf{k}_{constrains}, \tag{A11}$$

where $\mathbf{k}_{constrains}$ represents the exact theoretical values required by the crystal family of S_g (e.g., ensuring 90° angles or equal edge lengths).

Coordinate Rectification via Subspace Projection. In the absence of hard constraints, the fractional coordinates $\mathbf{F}_t \in \mathbb{R}^{N \times 3}$ generated at step t inevitably violate the strict site symmetries. We employ a *Project-and-Reconstruct* mechanism to rectify $\mathbf{F}_t$ into a symmetry-compliant state $\hat{\mathbf{F}}_t$.

For each Wyckoff orbit w identified in $\mathbf{l}^*$, let $\mathcal{I}_w$ be the set of atom indices belonging to this orbit. The positions of these atoms are geometrically related via affine transformations $\{(\mathbf{R}_n, \mathbf{t}_n)\}_{n \in \mathcal{I}_w}$. We perform the rectification in two substeps:

First, we aggregate the fractional coordinates $\mathbf{F}_t$ at the current denoising step t to estimate a robust canonical base coordinate $\mathbf{F}'_t$ (representing the generator of the orbit). This is formulated as a least-squares problem minimizing the deviation from symmetry operations. The optimal solution is computed via the Moore-Penrose

Algorithm 1: Constrained Beam Search with Matrix-based State Tracking

Input: Probability distribution p_w (from Eq. 2), Space group S_g, Atomic sequence $C_{\text{atoms}} = [A, \ldots, B, \ldots]$, Unique elements $\mathcal{E}$.
Output: Optimal assignment sequence $\mathbf{l}^*$.

```
// --- Phase 1: Initialization ---
Set Beam Width K, L_valid ← L(S_g)
// Initialize state at step 0: empty list, zero score, zero matrix
B_0 ← {(∅, 0, 0_{|E|×|L_valid|})},   l* ← None,   s* ← −∞
// --- Phase 2: Iterative Search ---
for n ← 1 to N do
    B_n ← ∅
    e_n ← C_atoms[n]                                   ▷ Element type of the n-th atom
    // Count remaining atoms of type e_n (Cardinality of the subset)
    N_rem ← |{k | n < k ≤ N, C_atoms[k] = e_n}|
    // Sort candidates by conditional probability for the n-th atom
    L_sorted ← Sort(L_valid) by p_w(l_n = l | C_atoms) descending
    for each hypothesis (l_{1:n−1}, s_{1:n−1}, Count_{1:n−1}) ∈ B_{n−1} do
        for each letter l ∈ L_sorted do
            // Update cumulative log-probability
            s_{1:n} ← s_{1:n−1} + log p_w(l_n = l | C_atoms)
            // Update counter matrix for step n
            Count_{1:n} ← Copy(Count_{1:n−1})
            Count_{1:n}[e_n, l] ← Count_{1:n}[e_n, l] + 1
            // Pruning: Check algebraic consistency
            c ← Count_{1:n}[e_n, l]
            m_req ← ⌈c / mult(l)⌉ × mult(l)
            if c + N_rem ≥ m_req then
                Add (l_{1:n−1}.append(l), s_{1:n}, Count_{1:n}) to B_n
    // Keep best K by score s_{1:n}
    B_n ← TopK(B_n, K)
// --- Phase 3: Final Selection ---
for each (l, s, Count) ∈ B_N do
    // Final Validation: All counts must be exact multiples
    is_valid ← ∀e ∈ E, l ∈ L_valid : Count[e, l] mod mult(l) = 0
    if is_valid and s > s* then
        l* ← l,   s* ← s
return l*
```

pseudoinverse:

$$\mathbf{F}'_t = \frac{1}{|\mathcal{I}_w|} \sum_{n \in \mathcal{I}_w} \mathbf{J}_w^{\dagger}(\mathbf{f}_{t,n} - \mathbf{t}_n), \tag{A12}$$

where $\mathbf{f}_{t,n}$ is the n-th row of $\mathbf{F}_t$, and $\mathbf{J}_w^{\dagger}$ is the pseudoinverse of the site-symmetry Jacobian matrix, projecting the coordinates onto the valid degrees of freedom (e.g., a specific axis or plane) defined by the Wyckoff letter.

Second, we strictly reconstruct the symmetry-compliant state $\hat{\mathbf{F}}_t$ by broadcasting the canonical base coordinate $\mathbf{F}'_t$ back to all equivalent atoms in the orbit. For each $n \in \mathcal{I}_w$, the rectified coordinate $\hat{\mathbf{f}}_{t,n}$ (the n-th row of $\hat{\mathbf{F}}_t$) is explicitly computed as:

$$\hat{\mathbf{f}}_{t,n} = \mathbf{R}_n \mathbf{F}'_t + \mathbf{t}_n. \tag{A13}$$

By simultaneously replacing the noisy states $\mathbf{k}_t$ and $\mathbf{F}_t$ with their rectified counterparts $\hat{\mathbf{k}}_t$ and $\hat{\mathbf{F}}_t$ at the end of each denoising step, we ensure that both the atomic configuration and the unit cell geometry strictly evolve on the geometric manifold defined by the target Wyckoff positions.

Appendix B: Hyper-parameters and Training/Inference Configurations

Gemini said This section details the implementation specifications for our proposed symmetry prediction method. For the generative diffusion backbone, we strictly adhere to the original configurations of DiffCSP++ [10]. We utilize its official open-source implementation with identical hyper-parameters, training schedules, and inference protocols, while replacing its CSPML-retrieved templates with our *ab initio* predicted Wyckoff templates to constrain its diffusion process. Ta-

ble III summarizes the hyper-parameters for the model architecture, and Table IV outlines the training and inference configurations.

Appendix C: Evaluation Metrics and Benchmark Datasets

C.1. Evaluation Metrics: The SUN and Matching Rate Metrics

Following the core principles of the protocol defined by Zeni et al. [14], we evaluate generative quality using the SUN metrics. Leveraging the low inference cost of our model, we adopt a Top-20 evaluation strategy: for each test composition, we generate 20 candidate structures. Each candidate is assessed against three criteria:

- **Stability**. A structure is classified as *stable* if its formation energy is within 0.1 eV/atom of the convex hull of competing phases. While Zeni *et al.* [14] employed density functional theory (DFT) for the final stability verification of 1,024 samples, performing DFT relaxations across the entire test set is computationally prohibitive under our extensive Top-20 evaluation setting. To ensure computational feasibility, we utilize MatterSim [29], an accurate machine learning force field method validated by Zeni *et al.* [14], as a high-fidelity surrogate for geometry optimization and energy evaluation.

- **Uniqueness**. A structure is considered *unique* if it is not structurally equivalent to any other sample within the generated batch of 20 candidates. Equivalence is determined using the robust structure matcher from Zeni et al. [14], which extends `pymatgen`'s `StructureMatcher` [30] to handle partial occupancies, elemental substitutions, and symmetry tolerances.

- **Novelty**. A structure is labeled *novel* if it is not structurally equivalent to any entry in the combined reference database. We construct this reference set by merging the Alexandria and MP-20 datasets [26, 31], yielding a comprehensive collection of 845,997 materials. The matching process permits up to a 10% deviation in elemental ratios to account for stoichiometric variability.

Accordingly, the Top-20 SUN score represents the success rate at the composition level. A composition is considered solved if at least one of its 20 candidates simultaneously satisfies the stability, uniqueness, and novelty criteria:

$$\text{Top-20 SUN} = \frac{N_{\text{stable}\cap\text{unique}\cap\text{novel}}@\text{Top-20}}{N_{\text{total}}} \times 100\%, \tag{C1}$$

where $N_{\text{stable}\cap\text{unique}\cap\text{novel}}$ is the number of test compositions that yielded at least one valid candidate satisfying all three conditions, and N_{total} is the total number of compositions in the test set.

Complementary to the SUN metrics, we employ the Top-20 Matching Rate to evaluate the model's ability to recover ground-truth structures. For each testing composition, we generate 20 candidates, recording a successful match if at least one candidate is structurally equivalent to the GT. Exactly following previous works [10, 19], this equivalence is evaluated via the `StructureMatcher` class in `pymatgen` using tolerances of stol = 0.5, angle_tol = 10°, and ltol = 0.3. The metric is then calculated as the percentage of matched compositions across the entire testing set:

$$\text{Top-20 Matching Rate} = \frac{N_{\text{matched}}@\text{Top-20}}{N_{\text{total}}} \times 100 \tag{C2}$$

The complementarity of Top-20 SUN and Top-20 Matching Rate lies in their distinct evaluative focuses: the SUN metric emphasizes discovery and viability, rewarding the model's capability to explore unknown chemical spaces and generate physically plausible materials that do not necessarily exist in the training distribution. Conversely, the Matching Rate measures reconstruction fidelity, quantifying how accurately the model can capture the underlying distribution of known experimental or high-quality DFT structures. Together, they provide a holistic reflection of the generative model's performance, balancing the requirement for creative exploration with the necessity of structural accuracy.

C.2. Benchmark Datasets

To ensure a fair comparison with the baseline method DiffCSP++ [10], we utilize the same three benchmark datasets with identical training, validation, and test splits.

- **MP-20** [26]: Comprising 45,231 experimentally verified materials from the Materials Project, this dataset includes diverse crystal systems with up to 20 atoms per conventional unit cell. It serves as a balanced benchmark for structural and compositional diversity.

- **Perov-5** [25]: A dataset containing 18,928 perovskite-type structures. Each unit cell contains exactly 5 atoms. This dataset provides a controlled environment for evaluating compositional generalization under a fixed topological constraint.

- **MPTS-52** [10]: A more challenging dataset consisting of 40,476 structures with up to 52 atoms per unit cell. It represents a broader sampling of the

TABLE III: Hyper-parameters for the model architecture.

Category	Parameter	Value
Data & Tensor Shapes	Batch Size (B)	32
	Max Sequence Length (L)	128
	Hidden Dimension (D)	256
	Wyckoff Labels (C)	25 (include `<pad>`)
Transformer Backbone	Layers (L_{depth})	6
	Attention Heads (H)	8
	Head Dimension (d_h)	32
	FFN Hidden Dimension	512
	Dropout Rate	0.15
SoftMoE	MoE Layers	All 6 layers
	Total Experts (E)	8
	Active Experts (k)	2 (Top-k Router)
	Capacity Factor	1.5
	Router Noise Std	0.5
Vocabulary Sizes	Element Tokens	90 (include `<pad>`, `<unk>`)
	Space Group Tokens (S_g)	231 (include `<unk>`)

TABLE IV: Training and inference configurations.

Hyperparameter	Value
Optimizer	AdamW
Learning Rate (LR)	1×10^{-4}
Weight Decay	0.01
Betas	(0.9, 0.98)
Epsilon	1×10^{-8}
Gradient Clipping	1.0
Scheduler	ReduceLROnPlateau
Factor / Patience	0.5 / 3
Threshold	5×10^{-4}
Min LR	1×10^{-6}
Max Epochs	200
Batch Size	32
Gradient Accumulation	4 steps
AMP (Mixed Precision)	Enabled
Early Stopping Patience	10 epochs
Beam Width (K)	100

complex real-world crystal structure space, testing the model's scalability to larger systems.